Helicobacter pylori Gpt targets SLC7A11 to trigger ferroptosis and promote chronic atrophic gastritis

Jingsen Yang[1,2#], Jingjing Wei[3,4#], Zheyao Hu[5#], Min Liu[1,2], Chao Zheng[1,2], Hao Zhang[1,2], Yanjing Xiang[1,2], Qinkun Wang[1,2], Jiayi Shen[1,2], Jordi Marti[6*], Zehao Zhuang[7*], Xu Lin[1,2*], Zhaowei Xu[1,2*]

[1]Key Laboratory of Gastrointestinal Cancer (Fujian Medical University), Ministry of Education, Fuzhou, China

[2]Department of Medical Microbiology, Fujian Key Laboratory of Tumor Microbiology, School of Basic Medical Sciences, Fujian Medical University, Fuzhou, China

[3]Department of Endoscopy, The First Affiliated Hospital, Fujian Medical University, Fuzhou, China

[4]Endoscopy Center, National Regional Medical Center, Binhai Campus of the First Affiliated Hospital, Fujian Medical University, Fuzhou, China

[5]Shanghai Center for Systems Biomedicine, Key Laboratory of Systems Biomedicine (Ministry of Education), Shanghai Jiao Tong University, Shanghai, China.

[6]Department of Physics, Polytechnic University of Catalonia-Barcelona Tech, Barcelona, Catalonia, Spain

[7]Department of Gastroenterology, The Second Affiliated Hospital, Fujian Medical University, Quanzhou, China

[#]These authors contributed equally to this study.

[*]Corresponding authors. E-mail: xuzw@fjmu.edu.cn (Zhaowei Xu), linxu@mail.fjmu.edu.cn (Xu Lin), zhuang203@yeah.net (Zehao Zhuang), jordi.marti@upc.edu (Jordi Marti)

Highlights

1. Established a *Helicobacter pylori* proteome microarray and identified Gpt as a novel pathogenic factor.
2. Elucidated the mechanism by which Gpt induces ferroptosis through modulation of SLC7A11.
3. Identified Gpt as a potential biomarker for atrophic gastritis risk stratification.

Abstract

Helicobacter pylori (*H. pylori*) infection is a major driver of gastric diseases, but with a global prevalence of nearly 50%, precise risk stratification among infected individuals remains challenging. Here, we constructed a comprehensive *H. pylori* proteome microarray encompassing 1,631 proteins and applied it to screen sera from patients with chronic atrophic gastritis (CAG), providing a practical entry point to dissect virulence-host interactions that shape disease progression. Through systematic screening, we identified glutamate pyruvate transaminase (Gpt) as a CAG-associated antigen. In independent validation cohorts, anti-Gpt IgG demonstrated high accuracy in distinguishing patients with CAG from those with chronic non-atrophic gastritis among *H. pylori*-infected individuals. Mechanistically, Gpt binds to the cystine/glutamate antiporter subunit SLC7A11 with nanomolar affinity (KD = 14.8 nM), destabilizing the SLC7A11-SLC3A2 heterodimer and thereby impairing cystine uptake. Consequently, Gpt reduces the antioxidant capacity of gastric epithelial cells by depleting glutathione, downregulating GPX4, and increasing lipid peroxidation, ultimately triggering ferroptosis. This ferroptotic phenotype is reversed by the ferroptosis inhibitor liproxstatin-1 and is markedly reduced during infection with a *gpt*-deficient *H. pylori* strain. Finally, in gastric biopsy samples from patients with CAG, Gpt expression spatially coincides with malondialdehyde accumulation, supporting *in vivo* activation of ferroptosis. These findings identify Gpt as a previously unrecognized *H. pylori* virulence factor that promotes CAG through ferroptosis, and they highlight anti-Gpt IgG as a promising noninvasive biomarker for risk stratification in *H. pylori* infection, enabling the identification of individuals at higher risk of progressing to precancerous gastric lesions.

Keywords: *Helicobacter pylori*, Chronic atrophic gastritis, Proteome microarray, Ferroptosis, Risk stratification

Introduction

Helicobacter pylori (*H. pylori*) is a Gram-negative, microaerophilic bacterium that chronically colonizes the human stomach and drives a wide spectrum of gastric diseases[1]. Globally, *H. pylori* infects roughly half of the population, remaining one of the most prevalent bacterial infections worldwide[2]. Epidemiological evidence indicates that 78.5% of non-cardia gastric cancer cases are attributable to *H. pylori* infection[3], and eradication therapy reduces gastric cancer incidence by 41.9%[4]. Nevertheless, only an estimated 1-3% of infected individuals eventually develop gastric cancer, highlighting marked heterogeneity in clinical outcomes[1]. Against this backdrop, whether population-wide eradication should be universally implemented remains debated[5], making risk stratification prior to cancer onset a pragmatic strategy to guide precision surveillance and therapy among infected individuals.

Chronic atrophic gastritis (CAG) represents a critical and actionable stage within the well-established Correa cascade[6-9], marking the pivotal transition from reversible inflammation to irreversible precancerous change[10]. The pathogenesis of *H. pylori*-induced CAG is characterized by sustained epithelial injury, inflammatory infiltration, and eventual glandular loss[10,11]. While repeated gastric epithelial cell damage is recognized as a central driver, the specific mechanisms and responsible bacterial factors remain inadequately defined[12]. Existing evidence

implicates pathways such as apoptosis and cellular senescence[13]. However, a direct causal link between a defined *H. pylori* virulence factor and a specific host damage pathway leading to atrophy is still missing[14]. This mechanistic gap limits our ability to identify high-risk infections at the CAG stage and develop targeted interception strategies[15]. Therefore, elucidating the precise molecular events by which *H. pylori* initiates irreversible epithelial damage is fundamental to advancing risk stratification and prevention.

Among identified *H. pylori* virulence factors, the CagA and VacA proteins are strongly correlated with the incidence of CAG[1,16]. Epidemiological studies have demonstrated that, in European populations, seropositivity for CagA is associated with a 3.52-fold increased prevalence of CAG, while seropositivity for VacA confers a 3.19-fold increase[17]. Corresponding figures in East Asian populations are somewhat lower, with 2.31-fold and 2.14-fold increases for CagA and VacA, respectively[18]. Notably, high positivity rates for CagA (82%) and VacA (78%) persist among patients with non-atrophic gastritis, and approximately 20% of CAG patients remain seronegative for both antibodies[18]. These findings collectively suggest that additional pathogenic factors, beyond CagA and VacA, significantly contribute to the initiation and progression of CAG[19].

To identify *H. pylori* virulence factors that could enable risk

stratification at the precancerous stage, we employed a systematic discovery approach. We constructed a *H. pylori* proteome microarray and screened it with sera from a well-defined clinical cohort. This strategy identified the bacterial protein glutamate pyruvate transaminase (Gpt) as a candidate whose serological response strongly distinguished patients with CAG from those with non-atrophic gastritis (CNG). We further validated that Gpt is preferentially expressed within CAG lesions. Mechanistic investigation revealed that Gpt directly binds to the host transporter SLC7A11, disrupting cystine metabolism and driving ferroptosis in gastric epithelial cells, a pathway linking specific bacterial virulence to pre-malignant tissue damage. Our findings thus unveil Gpt as both a key mediator of pathogenesis and a promising biomarker, providing a molecular basis for stratifying *H. pylori*-infected individuals based on their risk of progressing to CAG.

Results

Construction of the *H. pylori* proteome microarray

To systematically profile the antigenic landscape of *H. pylori*, we began with two reference strains (26695 and J99) based on their complete genome annotations. We then constructed a recombinant expression library covering all 1,631 predicted open reading frames. **(Figure 1A)**. Following standardized induction and affinity purification, we

successfully obtained 1,420 soluble recombinant proteins. SDS-PAGE analyses confirmed their expected molecular weights and purity levels suitable for high-throughput screening, achieving coverage of approximately 87% of the target proteome **(Figure 1B)**, among the highest reported in comparable *H. pylori* studies to date. These proteins were printed in triplicate onto surface-activated glass slides, generating high-density microarrays. Quality control assays demonstrated excellent spot morphology, with no tailing, satellite spots, or signal heterogeneity, confirming the structural integrity of the microarray **(Figure 1C)**. Functionally, the microarrays were probed with sera from *H. pylori*-infected patients using IgG, IgM, and IgA detection channels, yielding strong, specific, and reproducible binding signals **(Figure 1D)**. This platform thus exhibits high sensitivity, specificity, and reproducibility, making it well-suited for large-scale antibody profiling and functional screening of pathogenic proteins.

Identification of Gpt as a potential pathogenic factor in CAG

To identify immunologically distinct antigens associated with CAG, we utilized the *H. pylori* proteome microarray to screen serum samples from 45 patients with chronic CNG and 45 patients with CAG, all selected from an endoscopic screening cohort with matched baseline characteristics **(Figure 2A, Table 1)**. Among tested proteins, Gpt exhibited significantly elevated antibody signals in the CAG group

compared to the CNG group ($p < 0.001$). In contrast, antibody responses to the classic virulence factor CagA showed no significant difference between the two groups, indicating that Gpt is a prominent immune-reactive antigen specifically associated with CAG progression **(Figure 2B)**. Subsequent validation using enzyme-linked immunosorbent assay (ELISA) on the same serum samples revealed that anti-Gpt IgG achieved an area under the receiver operating characteristic curve (AUC) of 0.94 (95% CI: 0.91-0.96), substantially higher than that of anti-CagA IgG (AUC = 0.66; 95% CI: 0.62-0.69) **(Figure 2C)**, confirming the superior diagnostic performance of anti-Gpt IgG for distinguishing CAG. Immunohistochemical analysis of independent gastric mucosal paraffin sections (CAG, n = 45; CNG, n = 45) further demonstrated significantly stronger staining for Gpt in CAG lesions compared to CNG tissues ($p < 0.01$), while CagA expression remained comparable between groups **(Figure 2D-E)**. Collectively, these consistent findings from protein microarray screening, serological validation, and histopathological assessment establish Gpt as a dominant antigen in CAG, highlighting its diagnostic superiority over CagA and strong potential for subsequent mechanistic investigations and translational applications.

Gpt interacts with the ferroptosis-related transporter SLC7A11

To elucidate the potential molecular mechanism of Gpt, we performed co-immunoprecipitation (Co-IP) coupled with mass spectrometry to

screen for Gpt-interacting proteins. Across two biological replicates, we identified a total of 17 candidate interacting proteins exhibiting enrichment fold-changes greater than 2 **(Figure 3A)**. Among these, the most prominent protein was SLC7A11, a key component of the ferroptosis-associated cystine/glutamate antiporter System Xc-. Notably, the co-component SLC3A2 met the detection threshold in only one replicate, suggesting a selective interaction between Gpt and SLC7A11. To validate this interaction, we employed Biolayer Interferometry (BLI) to determine the binding affinity between purified recombinant proteins. The equilibrium dissociation constant (KD) for the Gpt-SLC7A11 interaction was determined to be 14.8 nM **(Figure 3B)**, indicating high-affinity binding in vitro. Furthermore, intracellular Co-IP assays were conducted by transfecting Flag-tagged Gpt or empty vector into human gastric epithelial GES-1 cells. SLC7A11 was co-precipitated exclusively from the Gpt-overexpressing group, not from the control group, thereby confirming their interaction in a cellular context **(Figure 3C)**. Collectively, these results support that Gpt directly interacts with the ferroptosis-related transporter SLC7A11.

All-atom simulations reveal that Gpt disrupts the SLC7A11-SLC3A2 heterodimer interface

To further elucidate the mechanism underlying Gpt's interaction with the System Xc-complex, we performed both Molecular Dynamics (MD)

simulations and Well-tempered Metadynamics (WTM) simulations at the all-atom level based on the resolved human heterodimeric structure (PDB: 7P9V), which consists of the light-chain transporter subunit xCT (encoded by SLC7A11) and the heavy-chain chaperone subunit 4F2hc (encoded by SLC3A2). Two simulation systems were constructed: an unbound (apo) system (namely system-1) and a Gpt-bound system (namely system-2).

WTM simulations were conducted under physiological conditions (310.15 K) for 5,463 ns in the system-1 and 5,227 ns in the system-2. The magnitude of the projection along the normal direction of the membrane's surface of the vector defined between the xCT-Cys158-Cα atom and the 4F2hc-Leu295-Cα atom (distance d) was selected as the collective variable (CV) to monitor conformational changes (**Figure S1A**). In the unbound system-1, three main basins (I, II and III) are well defined in the one-dimensional free energy landscapes **(Figure 4A, Figure S1B-C)**. The most stable conformation is distributed in the minimum I, which corresponds to the native crystal structure and biological function ($d \approx 1.5$ nm). The free energy barriers required to move 4F2hc away from the cell membrane surface (minima II and III $d \approx 4.0$ to 4.4 nm) are around 26 kJ/mol **(Figure 4B)**. This indicates that, comparing with the open conformations (minima II and III), the structure of 4F2hc tends to the compact conformation (minimum I) **(Figure 4C)**.

In contrast, the Gpt-bound system (system-2) displayed multiple stable states (minima IV, V, VI and VII), and the lowest free energy basin was located at minimum VII (d ≈ 4.2 nm) **(Figure 4D, Figure S1D-E)**. The minima VI and VII correspond to 4F2hc being away from the cell membrane surface **(Figure 4E)**. The minimum V corresponds to 4F2hc close to the original position in crystal structure, whereas the minimum IV corresponds to 4F2hc departing from its original position and anchoring to the cell membrane. The free energy barriers required for the conversion between minima V and IV are approximately 16 kJ/mol and the highest free energy barriers for the conversion between minima V and VII are approximately 26 kJ/mol. This means that the binding of Gpt to the cell membrane will force 4F2hc to be located away from the cell membrane surface, although it can also keep some contact with cell membrane surface **(Figure 4F)**. Overall, the above results indicate that Gpt can bind to the xCT-4F2hc interaction interface and disturb the xCT-4F2hc interaction, further disrupting the normal physiological functions of xCT.

Further contact frequency analysis was employed to quantify the interaction interface between Gpt and xCT. The contact frequency results demonstrated that Gpt formed a stable, high-frequency interaction network with xCT, involving key residues such as Asn314 (100%), Gly313 (97.6%), Leu312 (92.5%), and Trp186 (91.4%) **(Figure 4G)**.

These residues are predominantly located at the channel entrance region of xCT, indicating that Gpt binding may directly interfere with substrate access.

Taken together, the MD simulations revealed at the atomic level that Gpt stably binds the SLC7A11 channel interface and disrupts the structural integrity of the SLC7A11-SLC3A2 heterodimer. This structural perturbation provides direct biophysical evidence supporting Gpt-mediated dysfunction of the System Xc- complex and its role in promoting ferroptosis.

Gpt induces ferroptosis in gastric epithelial cells

To investigate the functional impact of Gpt on gastric epithelial cells, we overexpressed Gpt in human gastric epithelial GES-1 cells. Under basal conditions, Gpt overexpression had minimal effects on cell viability. However, upon exposure to 10 μM erastin, Gpt-overexpressing cells exhibited a significant ~40% decrease in viability compared with vector controls. This inhibitory effect was further exacerbated with 40 μM erastin, indicating a dose-dependent response **(Figure 5A)**. To determine the specific cell-death pathway involved, we evaluated the effects of distinct pathway inhibitors. The ferroptosis inhibitor liproxstatin-1 effectively rescued Gpt-induced cell viability loss, whereas the pan-caspase inhibitor Z-VAD-FMK and the necroptosis inhibitor necro-sulfonamide provided no significant protection **(Figure 5B)**. These

results suggest that Gpt predominantly induces ferroptosis rather than apoptosis or necroptosis. Further assays assessing intracellular antioxidant status revealed that Gpt overexpression significantly decreased glutathione (GSH) levels and elevated malondialdehyde (MDA) concentrations, a key marker of lipid peroxidation **(Figure 5C-D)**, indicative of impaired antioxidant defenses. Mechanistically, although Gpt overexpression resulted in slight upregulation of SLC7A11 likely as a compensatory response expression of GPX4, a critical antioxidant enzyme, was markedly downregulated at both mRNA and protein levels **(Figure 5E-F)**, thereby enhancing cellular susceptibility to ferroptosis.

To validate the physiological relevance of Gpt during *H. pylori* infection, we infected GES-1 cells with either wild-type (WT) or *gpt*-knockout (Δ*gpt*) *H. pylori* strains. WT infection significantly reduced cell viability and increased MDA levels; these effects were notably attenuated in Δ*gpt*-infected cells **(Figure 5G-H)**. Moreover, liproxstatin-1 partially restored cell viability in WT-infected cells but had minimal effects on the Δgpt-infected group. Collectively, these results demonstrate that Gpt compromises antioxidant capacity, promotes lipid peroxidation, and induces ferroptosis in gastric epithelial cells in both overexpression and bacterial infection models. These findings further support the role of Gpt as a key pathogenic factor contributing to the progression of chronic atrophic gastritis.

Gpt is associated with ferroptosis activation in CAG lesions and exhibits diagnostic potential

To explore the relationship between Gpt expression and ferroptosis activation in clinical samples, we performed immunohistochemical staining for malondialdehyde (MDA), a key marker of lipid peroxidation, in an independent gastric biopsy cohort (CNG, n = 45; CAG, n = 45). Results demonstrated significantly stronger MDA staining intensity in CAG tissues compared with CNG tissues **(Figure 6A-B)**, indicating pronounced ferroptosis-associated oxidative stress in atrophic lesions. Furthermore, quantitative analysis revealed a positive correlation between Gpt expression intensity and MDA levels in CAG samples **(Figure 6C)**, suggesting a close spatial association between Gpt expression and ferroptosis signaling activation within diseased mucosa.

To evaluate the diagnostic potential of Gpt at the serological level, we measured anti-Gpt IgG levels in a separate serum cohort comprising CNG (n = 100) and CAG (n = 100) cases. Receiver operating characteristic (ROC) curve analysis showed that anti-Gpt IgG effectively discriminated CAG from CNG, yielding an area under the curve (AUC) of 0.879(95% CI: 0.841-0.893), significantly outperforming the commonly used serological marker PGI/II ratio (AUC = 0.721) **(Figure 6D)**. These findings collectively indicate that Gpt expression is tightly associated with ferroptosis signaling activation in CAG lesions and suggest that the

serological antibody response against Gpt holds promise as a sensitive and noninvasive biomarker for the early detection of chronic atrophic gastritis.

Discussion

In this study, a proteome-based serological screen identified the *H. pylori* protein Gpt as a novel virulence factor linked to CAG. We show that Gpt directly binds to and inhibits the cystine/glutamate antiporter SLC7A11, triggering glutathione depletion, lipid peroxide accumulation, and ferroptosis in gastric epithelial cells. Clinically, anti-Gpt IgG demonstrates promise as a serological biomarker for CAG. These findings reveal a direct mechanism by which a bacterial factor dysregulates a key ferroptosis pathway, advancing our understanding of *H. pylori*-induced gastric pathogenesis.

H. pylori pathogenesis is driven by well-established virulence factors such as CagA and VacA[1]. However, classical antigens like CagA show limited disease-stage specificity for instance, in our patient cohort CagA seropositivity did not differ between chronic non-atrophic and atrophic gastritis. In contrast, this study identifies Gpt as a novel *H. pylori* virulence protein uniquely associated with CAG. Serological responses against Gpt were significantly elevated in CAG patients compared to non-atrophic gastritis, and anti-Gpt IgG demonstrated superior diagnostic

accuracy for CAG relative to anti-CagA, underscoring Gpt's enhanced disease specificity and immunoreactivity. Mechanistically, Gpt was found to directly bind the host cystine/glutamate antiporter subunit SLC7A11, a key transporter in ferroptosis regulation and to disrupt the assembly of the SLC7A11-SLC3A2 heterodimer. This interference with cystine transport skews the intracellular redox balance: Gpt-expressing gastric epithelial cells exhibited impaired glutathione metabolism alongside excessive lipid peroxidation. Consistent with ferroptosis[20], Gpt-triggered cell death was specifically rescued by the ferroptosis inhibitor liproxstatin-1, whereas neither caspase inhibition nor necroptosis blockade conferred protection. Furthermore, infection experiments confirmed that *gpt*-deficient *H. pylori* induced significantly less oxidative damage and cell death than wild-type strains, and only wild-type infection was mitigated by liproxstatin-1 treatment. These findings reveal ferroptosis as a novel host-pathogen interaction axis exploited by *H. pylori* and highlight it as a promising therapeutic target, a druggable vulnerability wherein pharmacological ferroptosis blockade can protect gastric epithelial cells from *H. pylori*-induced injury.

The Vibrio parahaemolyticus effector VopQ inserts into lysosomal membranes to form gated pores that disrupt host ion homeostasis[21,22] and *H. pylori*'s VacA toxin oligomerizes into anion-selective channels in host cell membranes, collapsing organellar ion gradients[23,24]. Viruses likewise

encode ion-channel proteins to modulate host ion flux, for example, rotavirus secretes NSP4, which acts as a Ca^{2+}-conducting channel that disturbs enterocyte Ca^{2+} homeostasis[25]. Other microbes indirectly manipulate host channels via enzymatic or trafficking interference, such as Vibrio cholerae secretes cholera toxin, an ADP-ribosyltransferase that constitutively activates host adenylate cyclase, elevating cAMP and hyperactivating the CFTR chloride channel to induce massive Cl^- secretion[26,27], while enteropathogenic E. coli uses effectors like NleA to block ion channel surface expression[28,29]. Notably, these strategies involve either creating nonspecific pores or modulating signaling pathways rather than directly disassembling a host channel complex. By contrast, our findings reveal a distinct mechanism: Gpt directly binds at the SLC7A11-SLC3A2 interface and destabilizes this cystine-glutamate antiporter's heterodimeric assembly. This form of functional suppression, a secreted bacterial factor physically wedging into a host transporter to abrogate its activity appears unprecedented, broadening our understanding of microbial virulence by uncovering a novel strategy for direct impairment of host ion transporter function.

CAG is a precancerous stage of gastric carcinogenesis, providing the histopathological milieu in which dysplasia and adenocarcinoma can eventually develop. However, current serological screening tools such as gastrin-17 (G17) and pepsinogen I/II (PGI/II) exhibit notable limitations:

their sensitivity and specificity for detecting CAG are only moderate, and their readouts can be skewed by factors like active Helicobacter pylori infection or variations in gastric acid secretion. Moreover, these biomarkers do not reliably stratify the severity of atrophic change, as most serologic approaches dichotomize atrophy status rather than distinguishing moderate versus severe lesions[10,30-36]. In this study, Gpt emerged as a novel serological marker with markedly improved diagnostic accuracy for CAG and Gpt achieved high sensitivity and specificity, outperforming traditional assays in our cohort. Notably, Gpt maintained robust performance independent of traditional confounders: unlike PGI/II and G-17, whose accuracy can be compromised by *H. pylori* status or gastric acid output[33-36], Gpt showed consistently high diagnostic values across subgroups, potentially enabling more precise stratification of *H. pylori* associated disease progression. These findings highlight Gpt's potential utility in population level screening for atrophic gastritis. Nonetheless, further validation in multicenter cohorts is required, and it remains to be determined whether Gpt can distinguish pathological mucosal atrophy from physiological age-related glandular atrophy.

Materials and Methods

Construction of the Comprehensive *H. pylori* Proteome Microarray

Two representative *Helicobacter pylori* strains (26695 and J99) with well-annotated genomes were selected. Based on the open reading frames (ORFs) from NCBI, a total of 1,631 genes were codon-optimized and synthesized (GenScript, China) or amplified via overlap-extension PCR. These were subcloned into prokaryotic expression vectors pGEX-4T-1 (GST tag) or pET-28a (His tag) and transformed into *E. coli* BL21 (DE3). Protein expression was induced with 0.1 mM IPTG at 18°C for 12 h at 200 rpm in LB medium. Recombinant proteins were purified in high-throughput via GST or His affinity chromatography and verified by SDS-PAGE and Western blot. Only proteins with >95% purity were included for array fabrication. Purified proteins were normalized to 0.1-0.5 mg/mL and printed in triplicate onto epoxy-coated glass slides (CapitalBio, Beijing) using an ArrayJet microarrayer. Arrays were incubated overnight at 4°C for immobilization and subjected to stringent quality control (QC) to ensure absence of satellite spots, streaking, or signal heterogeneity.

Clinical Samples and Ethical Approval

All clinical samples were derived from the Fujian Gastric Disease Cohort. Gastric mucosal biopsies and serum samples were collected from patients diagnosed with chronic non-atrophic gastritis (CNG) or chronic atrophic gastritis (CAG) via endoscopic histopathology. Groups were matched for age, sex, *H. pylori* eradication history, and geographic origin. The study

included 45 CAG and 45 CNG patients, with written informed consent obtained from all participants. The study protocol was approved by the Ethics Committee of the First Affiliated Hospital of Fujian Medical University.

Antibody Profiling with Protein Microarray

Serum samples were diluted 1:200 in PBST (PBS + 0.1% Tween-20) and incubated overnight at 4°C with blocked protein microarrays (5% BSA in PBS). After three 5-minute washes in PBST, secondary antibodies (anti-human IgG, IgA, and IgM, all at 1:1,000; Jackson 109-165-008, 309-545-011, 709-605-073) were added and incubated for 1 h at room temperature. Arrays were scanned using a GenePix 4300A scanner (Molecular Devices) at 635/532 nm. Data were analyzed with GenePix Pro 7.0. Candidate antigens were defined as those with ≥2-fold signal intensity difference between groups and FDR < 0.05.

ELISA Validation

Purified Gpt protein was coated on 96-well ELISA plates (100 μL/well, 4°C overnight). After blocking with 5% BSA (2 h at 37°C), 1:100 diluted serum samples were incubated at 37°C for 30 min. After washing, HRP-conjugated anti-human IgG (1:5,000; Jackson ImmunoResearch) was added and incubated for 30 min. TMB substrate (Thermo Fisher) was used for color development, and reactions were stopped with 2 M H_2SO_4. Absorbance at 450 nm was read on a microplate reader (BioTek).

Diagnostic performance was evaluated via ROC curve, AUC, sensitivity, and specificity.

Immunohistochemistry (IHC)

Biopsy tissues were fixed in 4% paraformaldehyde, paraffin-embedded, and sectioned (4 μm). After deparaffinization and rehydration, antigen retrieval was performed in citrate buffer (pH 6.0), followed by quenching endogenous peroxidase with 3% H_2O_2. Sections were incubated overnight at 4°C with primary antibodies against Gpt, CagA, SLC7A11, MDA, and GPX4 (Abcam, 1:200 dilution), followed by biotinylated secondary antibodies and DAB staining. Five random fields per sample were analyzed, and expression intensity was quantified as H-score using ImageJ.

Cell Culture and Transfection

GES-1 human gastric epithelial cells were cultured in RPMI-1640 medium supplemented with 10% fetal bovine serum (FBS) and 1% penicillin-streptomycin (Gibco) at 37°C in 5% CO_2. The Gpt gene was cloned into pcDNA3.1-Flag vector (Invitrogen) and transfected using Lipofectamine 3000 (Thermo Fisher) according to the manufacturer's protocol. Protein expression was validated by Western blot 48 h post-transfection.

Co-immunoprecipitation (Co-IP) and Mass Spectrometry

GES-1 cell lysates were incubated overnight with anti-Flag (Sigma) or anti-Gpt antibody-conjugated magnetic beads. Beads were washed and eluted complexes were separated by SDS-PAGE, silver-stained, and subjected to LC-MS/MS analysis. Candidate interactors with >2-fold enrichment in both biological replicates were shortlisted for validation by Western blot or Bio-layer Interferometry (BLI).

Molecular Dynamics (MD) Simulations

To investigate the impact of Gpt binding on the human cystine/glutamate antiporter system xCT-4F2hc, we conducted all-atom molecular dynamics (MD) simulations based on the established protocol from Hu *et al*. (2025). Initial systems were prepared using the crystal structure of xCT-4F2hc (PDB: 7P9V), with Gpt predicted by AlphaFold; each system was embedded in an anionic membrane composed of 100% POPC lipids (upper/lower leaflet counts detailed in Table 1), fully solvated with TIP3P water molecules in a 0.15 M potassium chloride solution, and parameterized with the CHARMM36m force field for lipid-protein interactions. Energy minimization was performed via steepest descents and conjugate-gradient steps until convergence (Fmax $\leq$ 1000 kJ/mol), followed by equilibration: first under NVT ensemble for 1 ns with positional restraints (1000 kJ mol^{-1} nm^{-2} on heavy atoms) using the Berendsen thermostat at 310.15 K, then under NPT ensemble for 4 ns with semi-isotropic Berendsen barostat at 1 atm. Unbiased production

runs were executed in GROMACS/2021 with 3 independent replicas per system (total 6 μs), employing a 2-fs time step, particle mesh Ewald method for electrostatic interactions (Coulomb radius: 1.2 nm), and Lennard-Jones cutoff at 1.2 nm. For enhanced sampling, well-tempered metadynamics (WTM) simulations were performed using GROMACS/2023-PLUMED 2.9.0, with a collective variable (CV) defined as the magnitude of the vector projection along the membrane normal direction between atoms "xCT-Cys158-Cα" and "4F2hc-Leu295-Cα" (distance d);WTM parameters included a Gaussian width of 0.2 nm, initial hill height of 1.2 kJ/mol, deposition stride of 1 ps, bias factor of 10, and simulation durations of 5463 ns for system-1 (xCT-4F2hc only) and 5227 ns for system-2 (xCT-4F2hc-Gpt complex); convergence was validated through time evolution of Gaussian hill heights (indicating decay to a quasi-flat profile) and block analysis of free-energy errors (reaching a plateau),with data analyzed using the R-package metadynminer for free-energy surface calculation and minima identification. Residue-residue contact frequencies were quantified as interactions where atomic distances were <4 Å, visualized in VMD and Chimera; computational resources were provided by the Barcelona Supercomputing Center (Grants BCV-2024-2-0005 and BCV-2025-2-0006).

Ferroptosis Functional Assays

Gpt-transfected GES-1 cell was treated with 10 or 30 μM Erastin (MedChemExpress) and assessed for viability using the CCK-8 assay (Dojindo). Cell death pathway inhibitors included Liproxstatin-1 (2 μM, ferroptosis), Z-VAD-FMK (10 μM, apoptosis), and Necrosulfonamide (10 μM, necroptosis). Cellular GSH and MDA levels were measured using commercial kits (Beyotime). GPX4 and SLC7A11 expression levels were analyzed by Western blot.

Statistical Analysis

Data were presented as mean ± standard deviation (SD) from at least three independent experiments. Group comparisons were performed using Student's t-test or one-way ANOVA. Statistical significance was set at $P < 0.05$. Diagnostic performance was analyzed via ROC curves and AUC using SPSS 25.0.

Ethical Approval

The study was approved by the Ethics Committee of Fujian Medical University (NO. 2022-120). The study was conducted in accordance with the ethical principles of the Declaration of Helsinki. Written informed consent was obtained from all individual participants included in the study.

Data and software availability

The crystal structure files, MD simulation files (input files, parameter files, topology files, etc.), and structures of xCT are available on the website https://github.com/Zheyao-Hu/xCT. Moreover, all the software packages used in this study were the official release versions without any modifications.

Author contributions

J.S.Y.: Data curation, Formal analysis, Validation, Methodology.

J.J.W.: Resources, Validation, Visualization.

Z.Y.H.: Data curation, Visualization, Writing-original draft.

M.L.: Validation, Visualization.

C.Z.: Resources.

H.Z.: Resources.

Y.J.X.: Resources.

Q.K.W.: Resources.

J.Y.S.: Resources.

J.M.: Supervision, Visualization, Formal analysis.

Z.H.Z.: Resources, Supervision, Writing-original draft.

X.L.: Funding acquisition, Supervision, Conceptualization, Writing-original draft, Writing-review & editing.

Z.W.X.: Conceptualization, Resources, Writing-original draft, Writing-review & editing, Project administration, Supervision, Funding

acquisition.

Disclosure and competing interest statement

The authors declare no competing interests.

Acknowledgements

This study was supported by the National Natural Science Foundation of China (Grant No. 32000027), the Fujian Province Key Technological Innovation Research and Industrialization Project, China (No. 2024XQ012), Fuzhou, Xiamen and Quanzhou National Independent Innovation Demonstration Zone Collaborative Innovation Platform Project, China (2024-P-004) and the Natural Science Foundation of Fujian Province, China (No. 2022J01197).

Figure legends

Figure 1. Construction of the *H. pylori* proteome microarray and quality control.

(A) Workflow for gene synthesis and high-throughput protein production. Open reading frames were synthesized, cloned into pGEX-4T-1, transformed into *E. coli* BL21(DE3), expressed, and purified by glutathione affinity to yield GST-tagged proteins. (B) Coomassie-stained SDS-PAGE of representative purified *H. pylori* proteins (lane labels are

ORF IDs; M, molecular-mass markers). (C) Quality control of the printed protein microarrays showing uniform spot morphology with triplicate features per protein (zoomed views at right). (D) Representative arrays probed with human sera; pseudo-colour composites demonstrate specific binding. Panel letters correspond to the figure; schematics are not to scale.

Figure 2. Anti-Gpt seroreactivity distinguishes chronic atrophic gastritis (CAG) from chronic non-atrophic gastritis (CNG) and aligns with tissue IHC.

(A) Heatmap of protein-microarray IgG signals across sera from chronic non-atrophic gastritis (CNG, n=45) and CAG (n=45). (B) Box plots of microarray signal intensity for Gpt and CagA in the same cohort (CNG n=45; CAG n=45). (C) Receiver-operating characteristic curves for ELISA-measured anti-Gpt and anti-CagA IgG on the 90 sera (AUC for Gpt = 0.942, 95% CI 0.922-0.961; AUC for CagA = 0.656, 95% CI 0.622-0.687). (D) Representative gastric biopsy sections stained by IHC for Gpt, CagA and *H. pylori* with H&E counterstaining; left, CNG; right, CAG; scale bars, 20 μm; magnified insets at right. (E) Quantification of tissue expression (H-score) for Gpt and CagA in independent biopsies (CNG n=45; CAG n=45). Box plots show the median (centre line), interquartile range (box) and 1.5× IQR whiskers; points indicate individuals. Data were analysed with two-sided Student's t-tests; exact n

values are indicated; see Methods for statistics.

Figure 3. Gpt physically binds the System Xc- subunit SLC7A11.

(A) Co-immunoprecipitation mass spectrometry screening plotted as fold change in two biological replicates; SLC7A11 and SLC3A2 are highlighted; candidates with FC>2 in both replicates are coloured. (B) Bio-layer interferometry (BLI) sensograms for purified Gpt binding to SLC7A11 at the indicated analyte concentrations; global fitting yields KD = 14.8 ± 2.1 nM, k_{on} = 1.81×10^{4} M^{-1} s^{-1} and k_{off} = 2.68×10^{-4} s^{-1}. (C) Co-IP validation in GES-1 cell transfected with Flag-Gpt or vector control: anti-Flag IP followed by immunoblotting detects endogenous SLC7A11 only in the Gpt group; input blots and molecular-mass markers (kDa) are shown. Blots are representative of three independent experiments.

Figure 4. All-atom simulations show that Gpt perturbs the xCT-4F2hc interface.

(A) One-dimensional free-energy profile (well-tempered metadynamics) for the apo xCT-4F2hc heterodimer along the collective variable d, defined as the projection onto the membrane normal of the vector from xCT-Cys158-Cα to 4F2hc-Leu295-Cα; minima I-III correspond to compact-to-open conformations. (B-C) Top and side views of the equilibrated apo structure embedded in a POPC bilayer. (D-F) As in A-C for the Gpt-bound system; multiple minima (IV-VII) indicate states in

612 which 4F2hc is displaced from the membrane interface. G, Close-up of
613 the Gpt-xCT interface highlighting residues with high contact frequency
614 (for example Asn314, Gly313, Leu312, Trp186, Ala318 and Phe197).
615 Metadynamics runs were 5.463 μs (apo) and 5.227 μs (Gpt-bound) at
616 310.15 K.

617 **Figure 5. Gpt promotes ferroptosis in gastric epithelial cells.**
618 (A) Cell viability (CCK-8) of GES-1 cell expressing Gpt or vector after
619 treatment with erastin (0-40 μM). (B) Viability of Gpt-expressing cells
620 treated with erastin (20 μM) together with inhibitors: liproxstatin-1 (2 μM;
621 ferroptosis), Z-VAD-FMK (10 μM; apoptosis) or necrosulfonamide (10
622 μM; necroptosis). (C) Intracellular GSH levels (percentage of vehicles).
623 (D) Cellular malondialdehyde (MDA; nmol/mg protein). (E) SLC7A11
624 mRNA abundance under the indicated conditions. (F) Immunoblots for
625 SLC7A11 and Gpt (β-actin loading control). (G) Cell viability in cells
626 infected with *H. pylori* wild-type (WT) or *gpt*-knockout (Δ*gpt*) strains in
627 the presence of erastin. (H) Inhibitor rescue during WT infection as in B.
628 Bars show mean ± s.d. from ≥3 independent experiments; one-way
629 ANOVA was used for multi-group comparisons (B-E, H) and two-sided
630 Student's t-tests for pairwise comparisons (A, G). *, $P<0.05$; **, $P<0.01$;
631 ***, $P<0.001$; ns, not significant. Exact n and P values are provided in the
632 Source Data.

633 **Figure 6. Ferroptosis signatures in CAG and diagnostic performance**

of anti-Gpt IgG.

(A) IHC staining for MDA in representative gastric biopsies from CNG and CAG with H&E; scale bars, 20 μm. (B) Box plots of relative MDA levels in CNG (n=45) and CAG (n=45). (C) Correlation between mucosal MDA and antral GSH levels (Pearson r=0.46, P<0.01). (D) ROC curves comparing serum anti-Gpt IgG with the pepsinogen I/II (PGI/II) ratio for distinguishing CAG from CNG in an independent cohort (CNG n=100; CAG n=100): AUC for anti-Gpt IgG = 0.879 (95% CI 0.841-0.893) versus PGI/II = 0.714 (95% CI 0.684-0.742). Box plots are defined as in Figure 2; statistics are two-sided; see Methods for details.

Supplementary Figure 1. Definition of the collective variable and convergence diagnostics for dynamics.

(A) Schematic of the xCT-4F2hc heterodimer embedded in a lipid bilayer showing the vector used to define the collective variable d (from xCT-Cys158-Cα to 4F2hc-Leu295-Cα) and its projection onto the membrane normal. (B, D) Time evolution of the deposited Gaussian hill height during WTM simulations for the apo and Gpt-bound systems, respectively. (C, E) Block-analysis estimates of the free-energy error as a function of block size for both systems, indicating satisfactory convergence.

References

1 Duan, Y., Xu, Y., Dou, Y. & Xu, D. Helicobacter pylori and gastric cancer: mechanisms and new perspectives. *Journal of Hematology & Oncology* **18**, doi:10.1186/s13045-024-01654-2 (2025).

2 Chen, Y.-C. *et al.* Global Prevalence of Helicobacter pylori Infection and Incidence of Gastric Cancer Between 1980 and 2022. *Gastroenterology* **166**, 605-619, doi:10.1053/j.gastro.2023.12.022 (2024).

3 Yang, L. *et al.* The relative and attributable risks of cardia and non-cardia gastric cancer associated with Helicobacter pylori infection in China: a case-cohort study. *Lancet Public Health* **6**, e888-e896, doi:10.1016/S2468-2667(21)00164-X (2021).

4 Yan, L. *et al.* Effect of Helicobacter pylori Eradication on Gastric Cancer Prevention: Updated Report From a Randomized Controlled Trial With 26.5 Years of Follow-up. *Gastroenterology* **163**, doi:10.1053/j.gastro.2022.03.039 (2022).

5 Price, A., Graham, D. Y. & Tan, M. C. Controversies regarding management of Helicobacter pylori infections. *Current Opinion in Gastroenterology* **39**, 482-489, doi:10.1097/mog.0000000000000981 (2023).

6 Alsina, M., Arrazubi, V., Diez, M. & Tabernero, J. Current developments in gastric cancer: from molecular profiling to treatment strategy. *Nat Rev Gastroenterol Hepatol* **20**, 155-170, doi:10.1038/s41575-022-00703-w (2023).

7 Wang, F.-H. *et al.* The Chinese Society of Clinical Oncology (CSCO): Clinical guidelines for the diagnosis and treatment of gastric cancer, 2021. *Cancer Commun (Lond)* **41**, 747-795, doi:10.1002/cac2.12193 (2021).

8 Correa, P. Human gastric carcinogenesis: a multistep and multifactorial process--First American Cancer Society Award Lecture on Cancer Epidemiology and Prevention. *Cancer Res* **52**, 6735-6740 (1992).

9 He, J. *et al.* Helicobacter pylori infection induces stem cell-like properties in Correa cascade of gastric cancer. *Cancer Lett* **542**, 215764, doi:10.1016/j.canlet.2022.215764 (2022).

10 Shah, S. C., Piazuelo, M. B., Kuipers, E. J. & Li, D. AGA Clinical Practice Update on the Diagnosis and Management of Atrophic Gastritis: Expert Review. *Gastroenterology* **161**, doi:10.1053/j.gastro.2021.06.078 (2021).

11 Plummer, M., Franceschi, S., Vignat, J., Forman, D. & de Martel, C. Global burden of gastric cancer attributable to Helicobacter pylori. *Int J Cancer* **136**, 487-490, doi:10.1002/ijc.28999 (2015).

12 Rosania, R. *et al.* Regulation of apoptosis is impaired in atrophic gastritis associated with gastric cancer. *BMC Gastroenterol* **17**, 84, doi:10.1186/s12876-017-0640-7 (2017).

13 Cai, Q. *et al.* Inflammation-Associated Senescence Promotes Helicobacter pylori-Induced Atrophic Gastritis. *Cell Mol Gastroenterol Hepatol* **11**, 857-880, doi:10.1016/j.jcmgh.2020.10.015 (2021).

14 Imai, S. *et al.* Helicobacter pylori CagA elicits BRCAness to induce genome instability that may underlie bacterial gastric carcinogenesis. *Cell Host Microbe* **29**, doi:10.1016/j.chom.2021.04.006 (2021).

15 Deng, Z. *et al.* The mechanisms of gastric mucosal injury: focus on initial chief cell loss as a key target. *Cell Death Discovery* **9**, 29, doi:10.1038/s41420-023-01318-z (2023).

16 Amieva, M. & Peek, R. M. Pathobiology of Helicobacter pylori-Induced Gastric Cancer. *Gastroenterology* **150**, 64-78, doi:10.1053/j.gastro.2015.09.004 (2016).

17 Gao, L., Weck, M. N., Michel, A., Pawlita, M. & Brenner, H. Association between chronic atrophic gastritis and serum antibodies to 15 Helicobacter pylori proteins measured by multiplex serology. *Cancer Res* **69**, 2973-2980, doi:10.1158/0008-5472.CAN-08-3477 (2009).

18 Cai, H. *et al.* Helicobacter pylori blood biomarker for gastric cancer risk in East Asia. *Int J Epidemiol* **45**, 774-781, doi:10.1093/ije/dyw078 (2016).

19 Hofer, M. *et al.* Accessible homeostatic gastric organoids reveal secondary cell type-specific host-pathogen interactions in Helicobacter pylori infections. *Nat Commun* **16**, 2767, doi:10.1038/s41467-025-57131-y (2025).

20 Tang, D., Chen, X., Kang, R. & Kroemer, G. Ferroptosis: molecular mechanisms and health implications. *Cell Res* **31**, 107-125, doi:10.1038/s41422-020-00441-1 (2021).

21 Peng, W. *et al.* A distinct inhibitory mechanism of the V-ATPase by Vibrio VopQ revealed by cryo-EM. *Nat Struct Mol Biol* **27**, 589-597, doi:10.1038/s41594-020-0429-1 (2020).

22 Sreelatha, A., Orth, K. & Starai, V. J. The pore-forming bacterial effector, VopQ, halts autophagic turnover. *Autophagy* **9**, 2169-2170, doi:10.4161/auto.26449 (2013).

23 Cover, T. L. & Blanke, S. R. Helicobacter pylori VacA, a paradigm for toxin multifunctionality. *Nat Rev Microbiol* **3**, 320-332 (2005).

24 Galmiche, A. & Rassow, J. Targeting of Helicobacter pylori VacA to mitochondria. *Gut Microbes* **1**, 392-395, doi:10.4161/gmic.1.6.13894 (2010).

25 Crawford, S. E. & Estes, M. K. Viroporin-mediated calcium-activated autophagy. *Autophagy* **9**, 797-798, doi:10.4161/auto.23959 (2013).

26 Gabriel, S. E., Brigman, K. N., Koller, B. H., Boucher, R. C. & Stutts, M. J. Cystic fibrosis heterozygote resistance to cholera toxin in the cystic fibrosis mouse model. *Science* **266**, 107-109 (1994).

27 Thiagarajah, J. R., Donowitz, M. & Verkman, A. S. Secretory diarrhoea: mechanisms and emerging therapies. *Nat Rev Gastroenterol Hepatol* **12**, 446-457, doi:10.1038/nrgastro.2015.111 (2015).

28 Thanabalasuriar, A., Koutsouris, A., Hecht, G. & Gruenheid, S. The bacterial virulence factor NleA's involvement in intestinal tight junction disruption during enteropathogenic E. coli infection is independent of its putative PDZ binding domain. *Gut Microbes* **1**, 114-118 (2010).

29 Burns, L., Le Mauff, F. & Gruenheid, S. Direct evidence of host-mediated glycosylation of NleA and its dependence on interaction with the COPII complex. *Gut Microbes* **16**, 2305477, doi:10.1080/19490976.2024.2305477 (2024).

30 Lorente, S., Doiz, O., Trinidad Serrano, M., Castillo, J. & Lanas, A. Helicobacter pylori stimulates pepsinogen secretion from isolated human peptic cells. *Gut* **50**, 13-18 (2002).

31 Zhang, T. *et al.* The potential value of serum pepsinogen and gastrin-17 for the diagnosis of chronic atrophic gastritis at different stages of severity: a clinical diagnostic study. *BMC Gastroenterol* **25**, 428, doi:10.1186/s12876-025-03996-8 (2025).

32 Zagari, R. M. *et al.* Systematic review with meta-analysis: diagnostic performance of the combination of pepsinogen, gastrin-17 and anti-Helicobacter pylori antibodies serum assays for the diagnosis of atrophic gastritis. *Aliment Pharmacol Ther* **46**, 657-667, doi:10.1111/apt.14248 (2017).

33 Zhou, J.-P. *et al.* Association of serum pepsinogens and gastrin-17 with Helicobacter pylori infection assessed by urea breath test. *Front Cell Infect Microbiol* **12**, 980399, doi:10.3389/fcimb.2022.980399 (2022).

34 Jung, D. H., Youn, Y. H., Jung, H.-K. & Lee, K. J. Predictors for the Development of Hypergastrinemia in Maintenance Treatment for Mild Gastroesophageal Reflux Disease Using a Half-dose Proton Pump Inhibitor. *J Neurogastroenterol Motil* **31**, 119-128, doi:10.5056/jnm24128 (2025).

35 Calam, J., Gibbons, A., Healey, Z. V., Bliss, P. & Arebi, N. How does Helicobacter pylori cause mucosal damage? Its effect on acid and gastrin physiology. *Gastroenterology* **113** (1997).

36 Liu, T. *et al.* A nanoparticle-based sonodynamic therapy reduces Helicobacter pylori infection in mouse without disrupting gut microbiota. *Nat Commun* **15**, 844, doi:10.1038/s41467-024-45156-8 (2024).

Table 1 | Baseline characteristics of study participants in the discovery (protein microarray) and validation (ELISA) cohorts

Cohort	Variable	CNG	CAG
Protein microarray (discovery, n=90)	Age, years (mean ± SD)	53.0 ± 7.9	52.2 ± 8.3
	Male, n (%)	22 (48.9)	18 (40.0)
	H. pylori positive, n (%)	45 (100.0)	45 (100.0)
ELISA validation (n=200)	Age, years (mean ± SD)	52.0 ± 8.6	52.4 ± 8.1
	Male, n (%)	51 (51.0)	51 (51.0)
	H. pylori positive, n (%)	100 (100.0)	100 (100.0)

Notes: Age values are expressed as mean ± standard deviation (SD). Categorical variables (sex and *H. pylori* infection) were compared using Fisher's exact test or chi-square test as appropriate.

Graphical Abstract

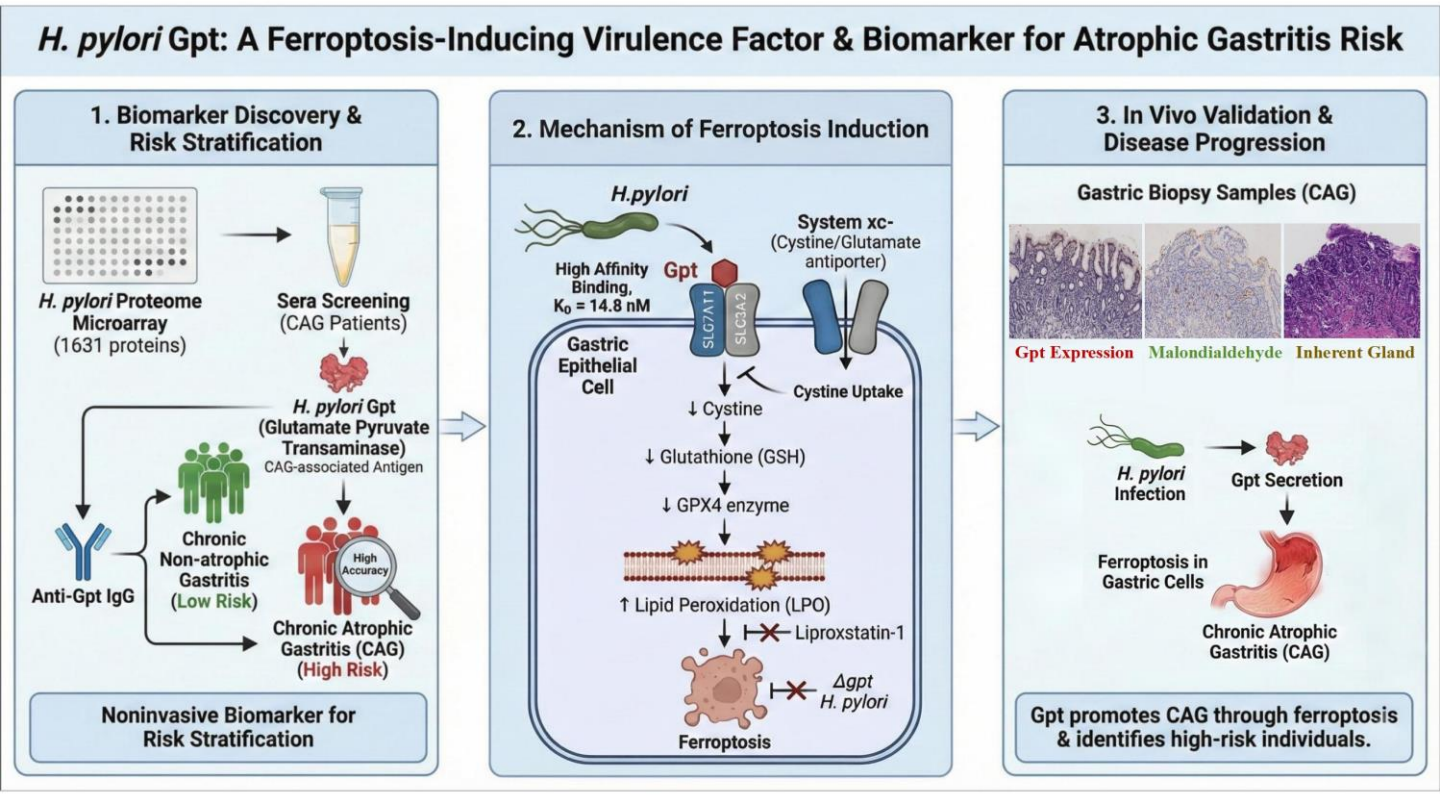

Figure 1

A.

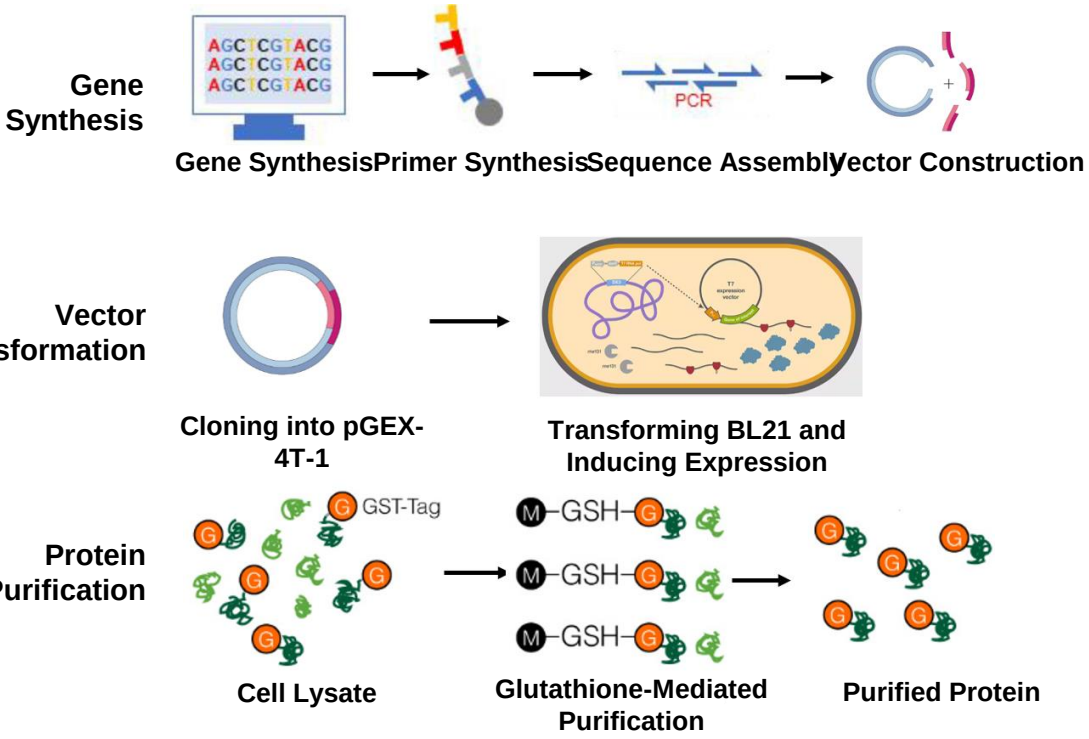

B.

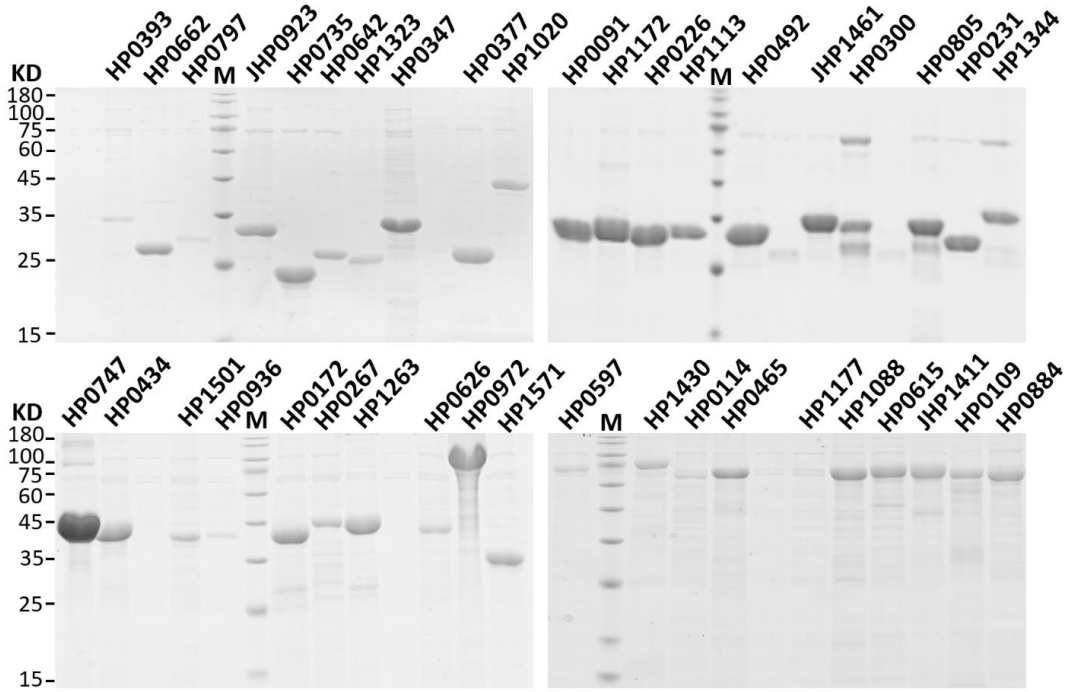

C.

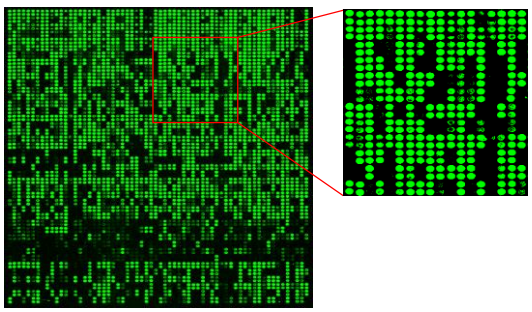

D.

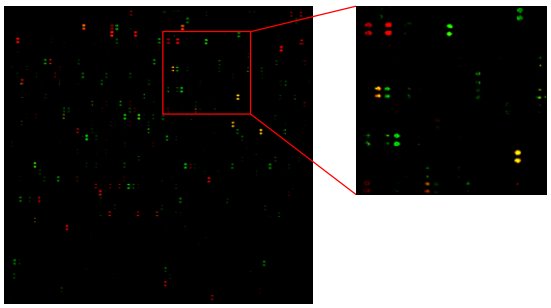

Figure 2

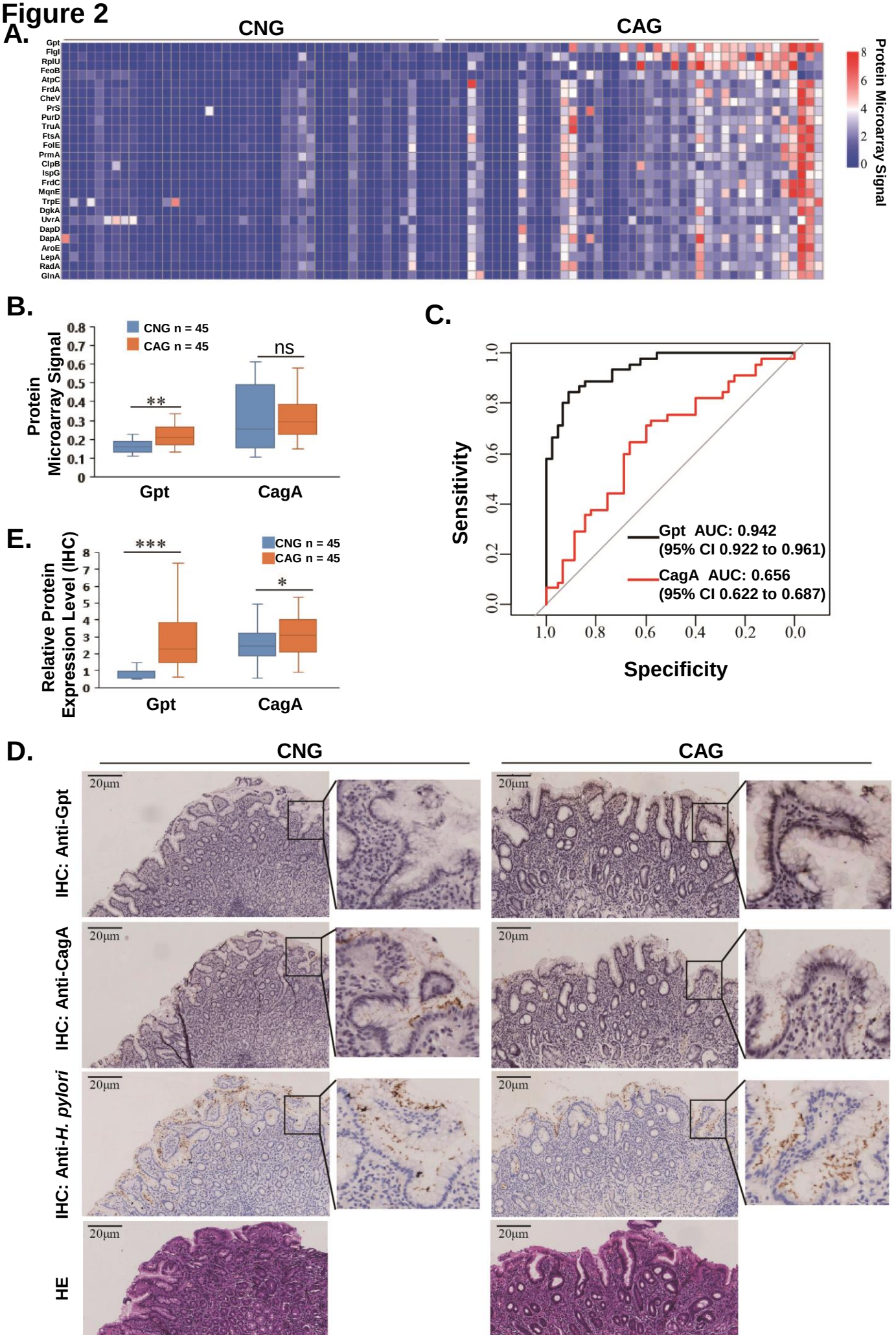
A.
CNG
CAG
Gpt
FlgI
RplU
FeoB
AtpC
FrdA
CheV
PrS
PurD
TruA
FtsA
FolE
PrmA
ClpB
IspG
FrdC
MqnE
TrpE
DgkA
UvrA
DapD
DapA
AroE
LepA
RadA
GlnA
Protein Microarray Signal
8
6
4
2
0
B.
Protein Microarray Signal
CNG n = 45
CAG n = 45
**
ns
Gpt
CagA
C.
Sensitivity
Specificity
Gpt AUC: 0.942
(95% CI 0.922 to 0.961)
CagA AUC: 0.656
(95% CI 0.622 to 0.687)
E.
Relative Protein Expression Level (IHC)
CNG n = 45
CAG n = 45
***
*
Gpt
CagA
D.
CNG
CAG
IHC: Anti-Gpt
IHC: Anti-CagA
IHC: Anti-H. pylori
HE
20μm

Figure 3

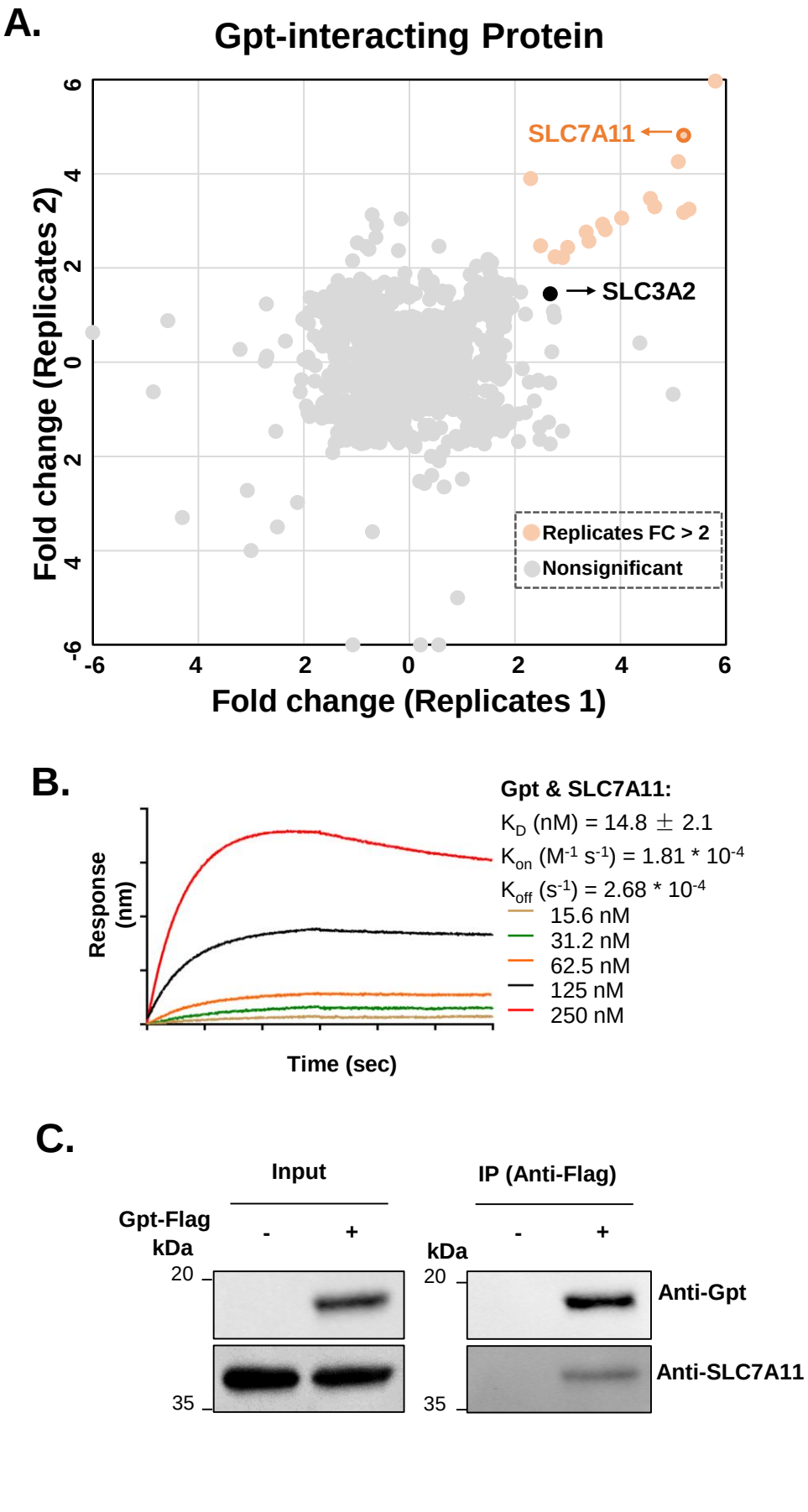
A.
Gpt-interacting Protein
SLC7A11
SLC3A2
Replicates FC > 2
Nonsignificant
Fold change (Replicates 2)
Fold change (Replicates 1)
B.
Gpt & SLC7A11:
K_D (nM) = 14.8 ± 2.1
K_on (M^-1 s^-1) = 1.81 * 10^-4
K_off (s^-1) = 2.68 * 10^-4
15.6 nM
31.2 nM
62.5 nM
125 nM
250 nM
Response (nm)
Time (sec)
C.
Input
IP (Anti-Flag)
Gpt-Flag
kDa
Anti-Gpt
Anti-SLC7A11

Figure 4

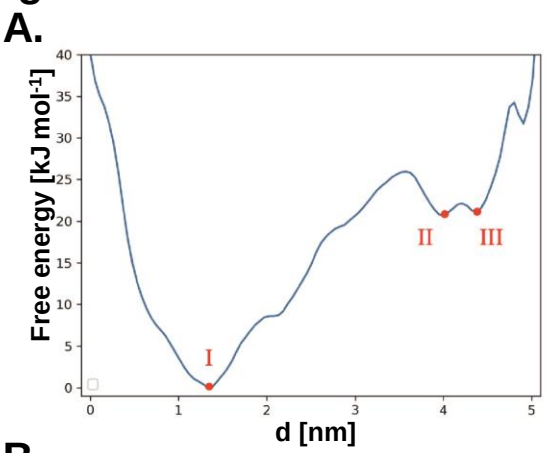
A.
Free energy [kJ mol-1]
d [nm]
I
II
III

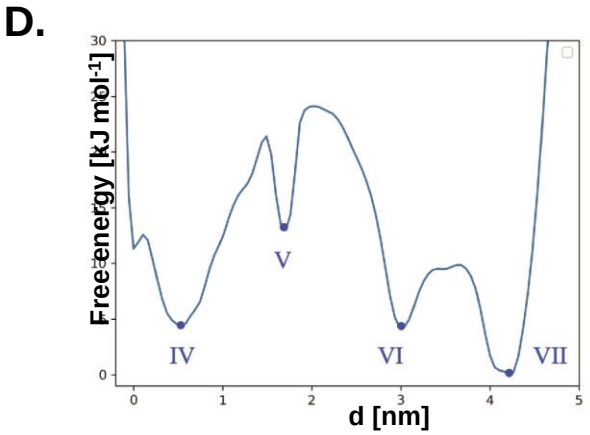
D.
Free energy [kJ mol-1]
d [nm]
IV
V
VI
VII

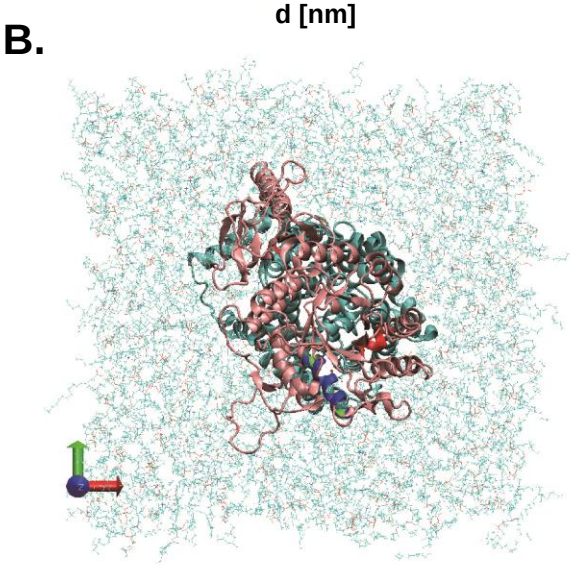
B.

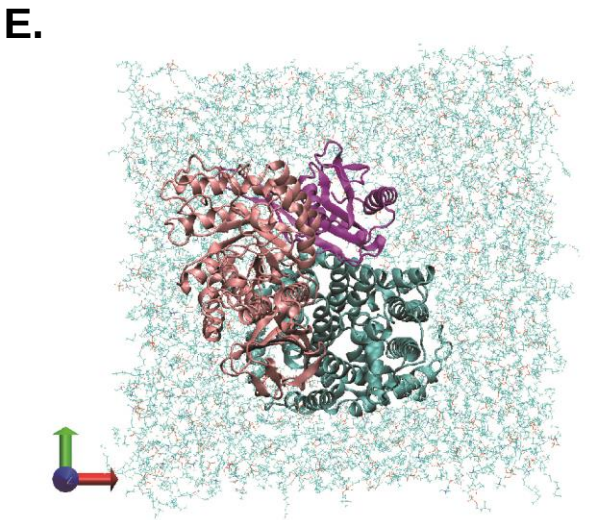
E.

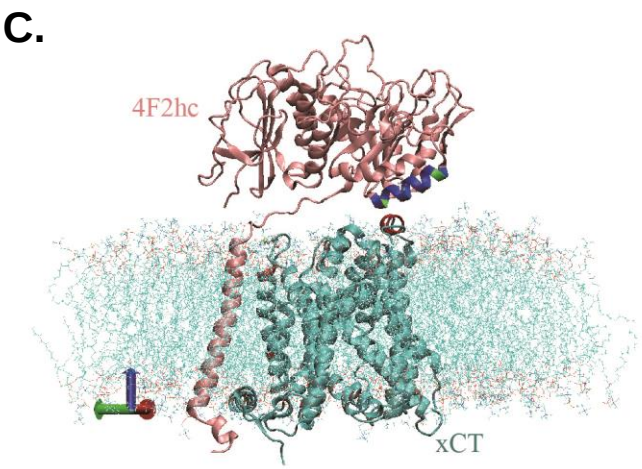
C.
4F2hc
xCT

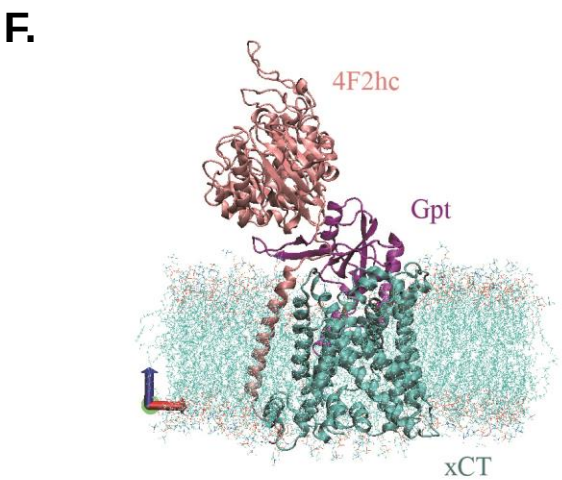
F.
4F2hc
Gpt
xCT

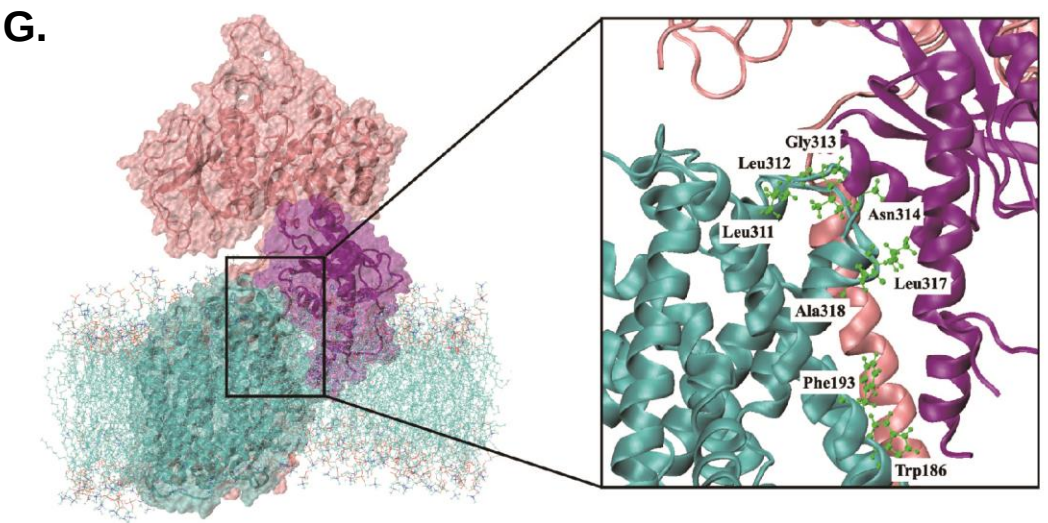
G.
Gly313
Leu312
Asn314
Leu311
Leu317
Ala318
Phe193
Trp186

Figure 5

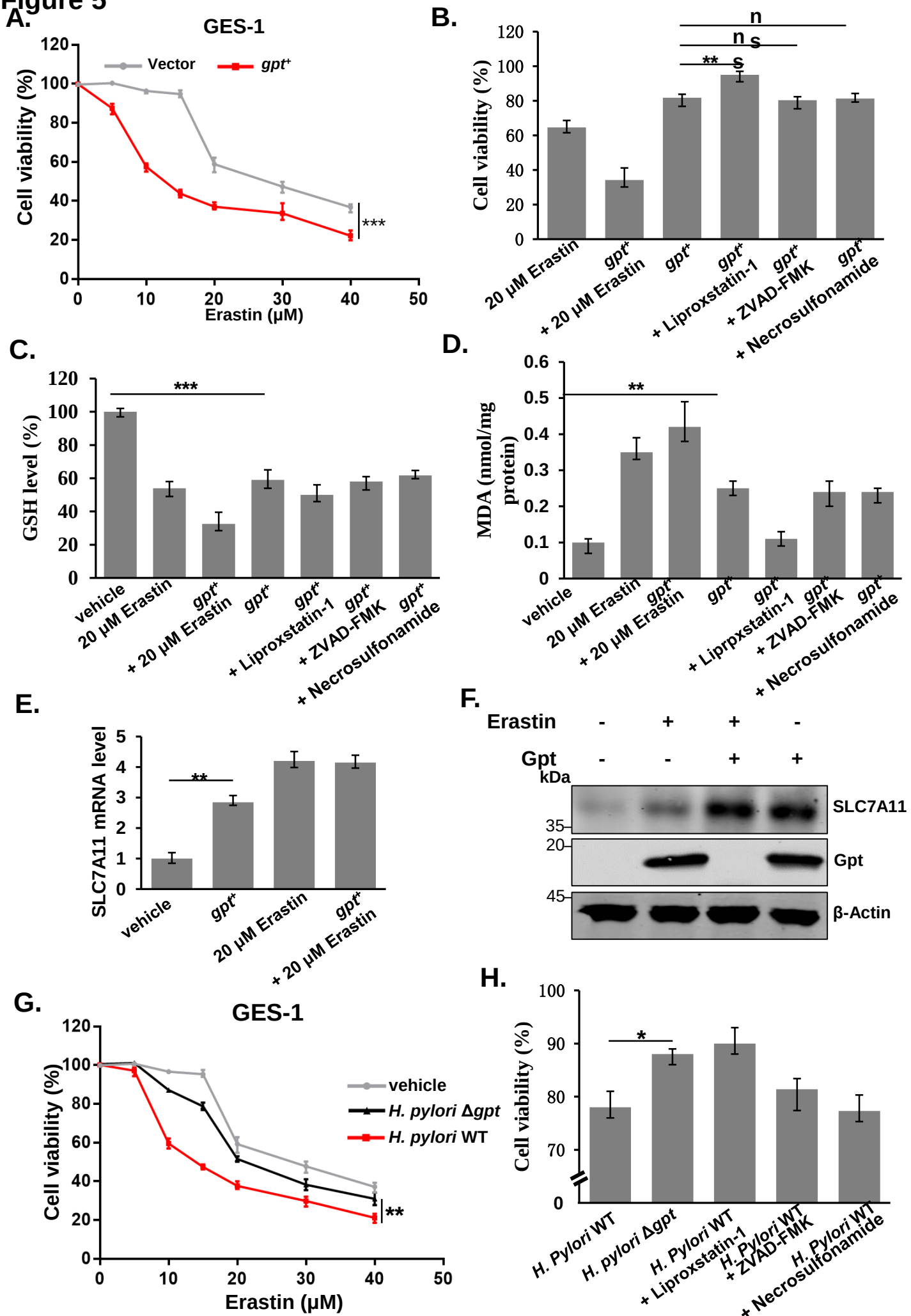
A.
GES-1
Vector
gpt+
Cell viability (%)
Erastin (μM)
***
B.
Cell viability (%)
n
n s
** s
20 μM Erastin
gpt+
gpt+ + 20 μM Erastin
gpt+ + Liproxstatin-1
gpt+ + ZVAD-FMK
gpt+ + Necrosulfonamide
C.
GSH level (%)
***
vehicle
20 μM Erastin
gpt+
gpt+ + 20 μM Erastin
gpt+ + Liproxstatin-1
gpt+ + ZVAD-FMK
gpt+ + Necrosulfonamide
D.
MDA (nmol/mg protein)
**
vehicle
20 μM Erastin
gpt+
gpt+ + 20 μM Erastin
gpt+ + Liprpxstatin-1
gpt+ + ZVAD-FMK
gpt+ + Necrosulfonamide
E.
SLC7A11 mRNA level
**
vehicle
gpt+
20 μM Erastin
gpt+ + 20 μM Erastin
F.
Erastin - + + -
Gpt - - + +
kDa
35
20
45
SLC7A11
Gpt
β-Actin
G.
GES-1
vehicle
H. pylori Δgpt
H. pylori WT
Cell viability (%)
**
Erastin (μM)
H.
Cell viability (%)
*
H. Pylori WT
H. pylori Δgpt
H. Pylori WT + Liproxstatin-1
H. Pylori WT + ZVAD-FMK
H. Pylori WT + Necrosulfonamide

Figure 6

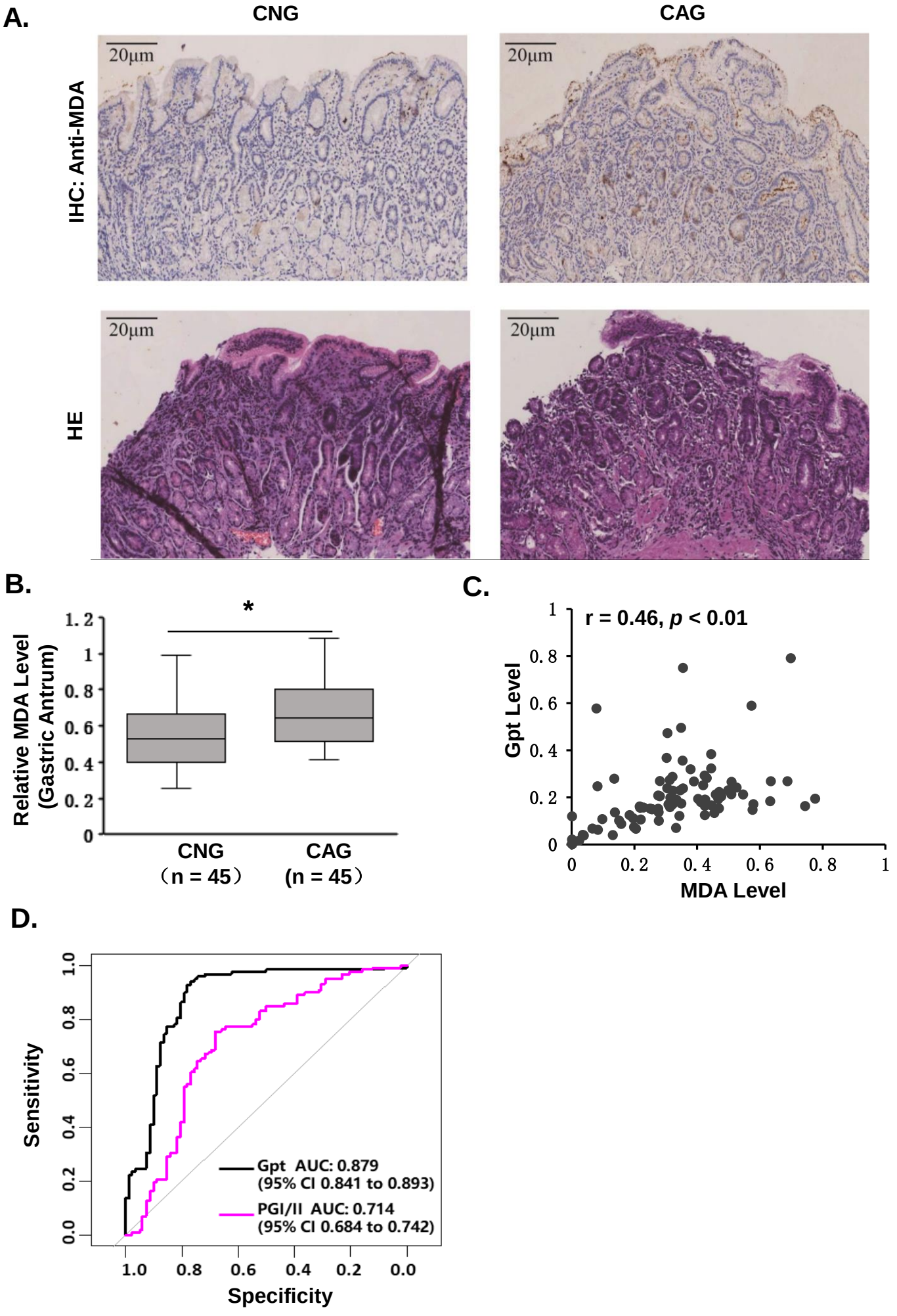
A.
CNG
CAG
IHC: Anti-MDA
HE
20μm
B.
*
Relative MDA Level (Gastric Antrum)
1.2
1
0.8
0.6
0.4
0.2
0
CNG (n = 45)
CAG (n = 45)
C.
r = 0.46, p < 0.01
Gpt Level
MDA Level
D.
Sensitivity
Specificity
Gpt AUC: 0.879 (95% CI 0.841 to 0.893)
PGI/II AUC: 0.714 (95% CI 0.684 to 0.742)

Table 1 | Baseline characteristics of study participants in the discovery (protein microarray) and validation (ELISA) cohorts

Cohort	Variable	CNG	CAG
Protein microarray (discovery, n=90)	Age, years (mean ± SD)	53.0 ± 7.9	52.2 ± 8.3
	Male, n (%)	22 (48.9)	18 (40.0)
	H. pylori positive, n (%)	45 (100.0)	45 (100.0)
ELISA validation (n=200)	Age, years (mean ± SD)	52.0 ± 8.6	52.4 ± 8.1
	Male, n (%)	51 (51.0)	51 (51.0)
	H. pylori positive, n (%)	100 (100.0)	100 (100.0)

Notes: Age values are expressed as mean ± standard deviation (SD). Categorical variables (sex and *H. pylori* infection) were compared using Fisher’s exact test or chi-square test as appropriate.